Iranian Journal of Pharmaceutical Sciences
2026: 22 (1): 418-432
https://journals.sbmu.ac.ir/IJPS

Research Article

OPEN ACCESS

A pH-responsive magnetic graphene oxide-based nanocomposite for doxorubicin delivery: adsorption and release kinetics studies

Seyyed Mostafa Hosseini[a], Parisa Miralinaghi[a]*, Mahsasadat Miralinaghi[b], Mohammadjavad Sohrabi [a]

[a] *Department of Pharmacy, Da.C., Islamic Azad University, Damghan, Iran.*
[b] *Department of Chemistry, VaP.C., Islamic Azad University, Varamin, Iran.*

Received: December 30, 2025 **Last Revision:** June 6, 2026 **Accepted:** August 5, 2026 **Available online:** November 1, 2026.

Abstract

Nanotechnology offers effective strategies for the development of controlled drug delivery systems, among which pH-responsive nanocarriers have received considerable attention due to their ability to modulate drug release in tumor-associated acidic environments while limiting systemic toxicity. In this study, a pH-responsive magnetic graphene oxide–based nanocarrier was fabricated for the loading and controlled release of doxorubicin (DOX). Carboxylated graphene oxide (CGO) was decorated with Fe_3O_4 nanoparticles, coated with polyvinylpyrrolidone (PVP), and subsequently functionalized with taurine (Tau) and glucosamine (Glu) to improve surface properties and drug–carrier interactions.

The structural, morphological, textural, and magnetic characteristics of the resulting Fe_3O_4@CGO–Tau/Glu nanosystem were investigated using FTIR, XRD, FE-SEM, BET/BJH, and VSM analyses. The results confirmed successful surface functionalization, preservation of the crystalline structure of Fe_3O_4, enhanced dispersion of magnetic nanoparticles, and a transition toward a more uniform mesoporous structure with increased specific surface area and pore volume. The nanocomposite exhibited superparamagnetic behavior, supporting its magnetic responsiveness.

The influence of pH on DOX adsorption was systematically examined, revealing a maximum loading efficiency at pH 8, attributed to electrostatic interactions between the negatively charged nanocarrier surface and the cationic form of DOX. Adsorption kinetics were best described by the pseudo-second-order model, suggesting that surface interactions dominate the loading process. In vitro release studies demonstrated pronounced pH-dependent release behavior, with faster and higher cumulative release under tumor-mimicking acidic conditions (pH 5.6) than under physiological pH (7.4). Nonlinear kinetic modeling showed that the Korsmeyer–Peppas and Peppas–Sahlin models provided the best fits to the release data, with analysis indicating that Fickian diffusion is the predominant rate-controlling mechanism, with a minor contribution from matrix relaxation or erosion.

The developed Fe_3O_4@CGO–Tau/Glu nanosystem demonstrates a favorable drug-loading capacity and pH-responsive release characteristics, highlighting its potential as a platform for controlled DOX delivery. Further investigations under more complex biological conditions are warranted to assess its biosafety, stability, and therapeutic performance.

Keywords: Adsorption; Kinetics; Release; pH-sensitive; Graphene oxide; Nanocomposite.

*** Corresponding Author**:
Parisa Miralinaghi, Department of Pharmacy, Da.C., Islamic Azad University, Damghan, Iran. E-mail: Parisa.Miralinaghi@iau.ac.ir.

Cite this article as: Hosseini S.M., Miralinaghi P., Miralinaghi M., Sohrabi M.J. A pH-responsive magnetic graphene oxide-based nanocomposite for doxorubicin delivery: adsorption and release kinetics studies. Iran. J. Pharm. Sci., 2026, 22 (1): 418-432.

DOI: https://doi.org/10.22037/ijps.v22i1.51173

This open-access article is distributed under the terms of the Creative Commons Attribution Non Commercial 4.0 License (CC BY-NC 4.0).

1. Introduction

Controlled release is an advanced technology in the development of drug delivery systems, improving therapeutic efficacy and reducing side effects by increasing the precision of drug delivery to target tissues. This technology has garnered considerable attention, particularly for the treatment of complex diseases such as cancer, diabetes, and cardiovascular disorders [1–3]. Targeted drug delivery systems can regulate the release process in response to biological or physical stimuli, aligning it with clinical requirements—a capability that distinguishes them from conventional approaches [4].

One such stimulus is pH variation in malignant tissues, caused by the abnormal metabolism of cancer cells, known as the *Warburg effect*. Unlike healthy cells, which primarily generate energy through cellular respiration and oxidative phosphorylation, malignant cells rely primarily on glycolysis, even under aerobic conditions. This results in the production of lactic acid, which lowers the pH around tumor cells, acidifying the tumor microenvironment [5]. This pH reduction is a key indicator for the development of pH-responsive nanocarriers, which are activated in acidic environments and release the drug selectively and in a controlled manner, facilitating targeted therapies [6].

DOX is a widely used drug for treating various cancers, particularly liver and breast cancers. One of the major challenges associated with DOX therapy is the development of drug resistance, which can lead to the failure of nearly 90% of chemotherapy treatments in metastatic cancers [7]. This resistance arises from increased expression of cell surface efflux pumps, such as the ATP-binding cassette family, or alterations in DNA repair pathways and programmed cell death mechanisms [8, 9]. In addition, DOX also affects healthy cells, and its administration is associated with adverse effects, including nausea, vomiting, bone marrow suppression, and arrhythmias. Moreover, evidence indicates that DOX can induce cardiac damage through increased oxidative stress, ultimately leading to cardiomyopathy [10, 11]. These limitations highlight the urgent need for designing intelligent drug delivery systems for DOX.

Graphene oxide (GO), with its unique physicochemical properties and planar structure, is considered an ideal nanocarrier for targeted drug delivery. The active functional groups and π-electrons on the surface of GO nanosheets enable covalent bonding with antibodies and cancer cell-targeting ligands [9, 10]. Surface modification of GO with magnetic nanoparticles enhances drug-loading efficiency (LE) and enables magnetic-field-guided delivery of the drug to tumor sites. However, the therapeutic efficacy of such multifunctional systems ultimately depends on how the drug interacts with the carrier and is released under appropriate physiological conditions. In a previous study, taurine (Tau)-functionalized graphene oxide (GO) was used to load 5-fluorouracil, achieving an encapsulation efficiency of 83.2% and a LE of 33.7% [12]. Furthermore, a pH-dependent release behavior of DOX from GO quantum dots–glucosamine (Glu)–boric acid was reported, with cumulative release of approximately 10% at pH 7.4 and 20% at pH 5.5 after 96 hours, confirming preferential drug release under acidic (tumor-like) conditions [13].

Understanding the mechanisms governing drug–carrier interactions and transport phenomena is crucial for optimizing drug delivery systems. Adsorption modeling provides quantitative insights into binding properties, surface heterogeneity, and the affinity between drug molecules and functional groups on the nanocarrier, which are essential for maximizing LE and preserving carrier stability. Simultaneously, release kinetic modeling allows for distinguishing between diffusion-controlled, swelling-driven, and relaxation-mediated release mechanisms, clarifying how environmental factors, such as pH, influence drug release [14]. Additionally, optimizing the pH as an adsorption parameter is crucial for maximizing LE and ensuring consistent release performance. These analyses facilitate accurate predictions of in vivo behavior and support the rational development of responsive drug delivery systems with controlled and predictable therapeutic outcomes.

Building on our previous work that demonstrated the synthesis and favorable biocompatibility of (Tau)/ Glu-functionalized carboxylate GO (CGO) nanocomposites [15], the present study investigates DOX LE and elucidates its pH-dependent release behavior. Tau, containing sulfonic acid and amine groups, was introduced to provide additional sites for hydrogen bonding and electrostatic interactions with DOX, while

This open-access article is distributed under the terms of the Creative Commons Attribution Non Commercial 4.0 License (CC BY-NC 4.0).

potentially improving hydrophilicity and colloidal behavior. Glu contributes hydroxyl and amine groups that can facilitate drug loading through hydrogen bonding. Moreover, Glu was included as a potential targeting ligand [16], intended to exploit the increased glucose uptake and overexpression of glucose transporters commonly observed in cancer cells. These modifications were designed to enhance drug loading efficiency and may support selective cellular internalization. The optimal pH for drug adsorption was determined, and the adsorption and release data under tumor-like and physiological pH conditions were analyzed using nonlinear kinetic models.

2. Materials and methods

2.1. Preparation of CGO

GO (0.5 g) was dispersed in deionized water, followed by the addition of 3.6 g of sodium hydroxide and 7 g of chloroacetic acid. The mixture was stirred at room temperature for 90 min to facilitate the carboxylation reaction. Subsequently, the suspension pH was adjusted to neutral with 10% HCl, and the resulting precipitate was collected by centrifugation. The product was washed several times with distilled water and ethanol to remove residual reagents and by-products, and then dried at 50 °C for 24 h to obtain CGO [17].

2.2. Preparation of Polyvinyl pyrrolidone-Coated Magnetic CGO (Fe_3O_4@CGO)

CGO (0.5 g) was dispersed in 125 mL of deionized water and sonicated for 1 h at room temperature to achieve uniform dispersion. Subsequently, 2.8 g ferric chloride hexahydrate ($FeCl_3 \cdot 6H_2O$), 1.03 g ferrous chloride tetrahydrate ($FeCl_2 \cdot 4H_2O$), and 0.33 g polyvinylpyrrolidone (PVP) were added to the suspension. The reaction was carried out under a nitrogen atmosphere and at reflux (80 °C), during which aqueous ammonia was added dropwise to maintain a pH of 10. Stirring was continued for 2 h to complete the co-precipitation process. Finally, the Fe_3O_4@CGO precipitate was separated by centrifugation, thoroughly washed with distilled water and ethanol, and dried at 50°C to obtain the PVP-coated magnetic CGO nanocomposite [18].

2.3. Preparation of Magnetic CGO Modified with Tau and Glu (Fe_3O_4@CGO─Tau/Glu)

To functionalize the surface of Fe_3O_4@CGO nanosheets with Tau and Glu, 0.75 g of Fe_3O_4@CGO was dispersed in 200 mL of double-distilled water under stirring. Subsequently, 0.75 g of 1-Ethyl-3-(3-dimethylaminopropyl) carbodiimide hydrochloride (EDC·HCl) and 1.1 g of N-Hydroxysuccinimide (NHS) were added to activate the carboxyl groups on the CGO surface. After 2 h of activation, 5 mL of Tau solution (0.1 g mL^{-1}) along with 0.3 g of Glu were introduced into the reaction mixture. The suspension was then continuously stirred for 24 h to allow covalent coupling. Finally, the resulting precipitates were collected by centrifugation and dried at 50°C [12]. The chemical stages of the synthesis procedure for the Fe_3O_4/CGO─Tau are illustrated in **Scheme 1**.

2.4. Determination of Zero Point of Charge (pH_{pzc})

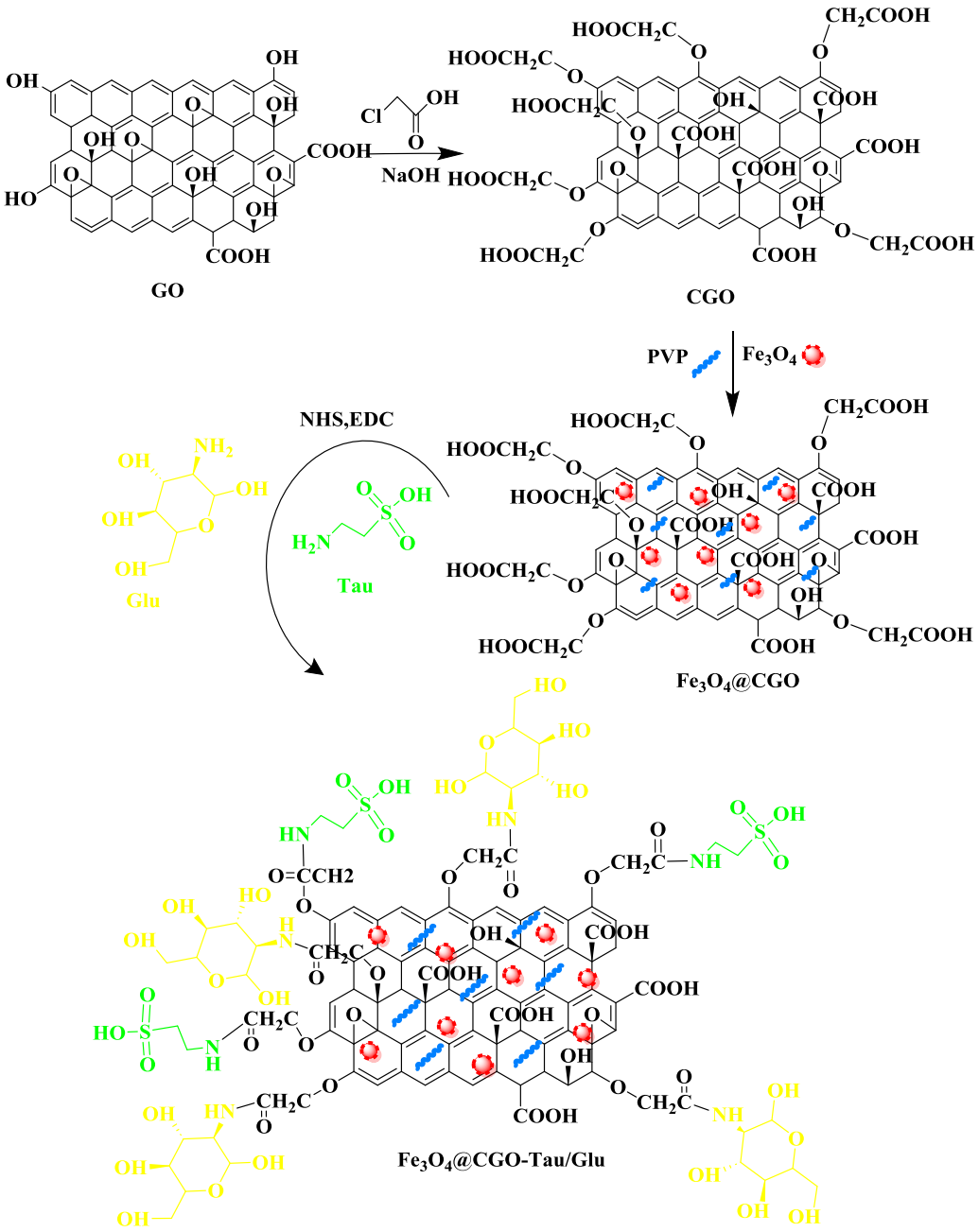
To determine the pH_{pzc}, 25 mL of 0.1 M NaCl solution was prepared with initial pH values ranging from 3 to 9, and 0.1 g of the adsorbent was added to each solution. The suspensions were stirred for 24 hours to reach equilibrium. The nanocomposite was then separated, and the final pH values of the samples were measured using a pH meter. The difference between the initial and final pH values was used to calculate the pH_{pzc} [19].

2.5. Effect of pH on Drug Adsorption

To investigate the effect of pH on the adsorption capacity of the adsorbent and drug LE, drug solutions with an initial concentration of 20 mg L^{-1} were prepared over a pH range of 3–9. In each experiment, 0.01 g of the adsorbent was added to 20 mL of the drug solution, and the resulting suspension was stirred for 120 min at 25 °C and 300 rpm to ensure sufficient contact between the drug and the adsorbent.

After completion of the adsorption process, the nanocomposite was separated by centrifugation, and the supernatant was filtered using a syringe filter. The residual drug concentration in the filtrate was determined using a UV–Vis spectrophotometer at the maximum absorption wavelength (λ_{max} = 480 nm).

This open-access article is distributed under the terms of the Creative Commons Attribution Non Commercial 4.0 License (CC BY-NC 4.0).



Scheme 1. Schematic illustration of the synthesis of Fe_3O_4@CGO–Tau/Glu

All experiments were performed in triplicate, and the results were reported as the mean ± 5% standard deviation. The adsorption capacity (q) and drug loading percentage were calculated using equations (1) and (2), respectively.

$$q_t = \frac{(C_0 - C_t)\,V}{W}$$

$$Drug\ loading(\%) = \frac{(C_0 - C_t)}{C_0} \times 100$$

Here, C_0 (mg L^{-1}) and C_t (mg L^{-1}) represent the drug concentrations at the beginning time and any time (t), respectively; V (L) is the volume of the drug solution, and W (g) is the mass of the adsorbent. To identify the dominant adsorption mechanism, the experimental data were fitted to the pseudo-first-order (PFO), pseudo-second-order (PSO), and intraparticle diffusion (IPD) kinetic models using a nonlinear regression approach in Mathematica (version 9.0).

This open-access article is distributed under the terms of the Creative Commons Attribution Non Commercial 4.0 License (CC BY-NC 4.0).

2.6. Adsorption kinetics studies

To understand the mechanism of the drug adsorption process, three common kinetic models, including the PFO model (Equation 3), PSO model (Equation 4), and IPD model (Equation 5), were fitted to the experimental adsorption data obtained at 5, 10, and 20 mg doses of the adsorbent [20].

$$\ln(q_e - q_t) = \ln q_e - K_1 t$$

$$dq/dt = K_2(q_e - q_t)^2$$

$$q_t = K_i\, t^{1/2} + C_i$$

Here, $q_{e,\mathrm{cal}}$ (mg g^{-1}) denotes the adsorption capacity at equilibrium, $q_{t,\mathrm{cal}}$ (mg g^{-1}) represents the amount of drug absorbed at time t, k_1 (min^{-1}) and K_2 (g mg^{-1} min^{-1}) are the rate constants of the PFO and PSO models, respectively. K_i (mg g^{-1} min$^{-1/2}$) is the intraparticle diffusion rate constant. C_i (mg g^{-1}) is the intercept related to boundary-layer thickness.

2.7. In vitro drug release study

For the drug release study, DOX was first loaded onto the nanomaterial at room temperature under the optimal pH conditions, and the release behavior was subsequently investigated at 37 °C and pH 7.4 and 6.5. Briefly, 0.20 g of Fe_3O_4@CGO–Tau/Glu was dispersed in 50 mL of an aqueous DOX solution with a concentration of 100 mg L^{-1}. The pH was adjusted to the optimal value (pH 8.0), and the mixture was stirred for 60 min at room temperature with a stirring speed of 300 rpm. The drug-loaded carrier was then separated using an external magnet and washed to remove unadsorbed DOX. The concentration of residual DOX in the supernatant was measured at the maximum absorption wavelength using a UV–Vis spectrophotometer.

To evaluate the in vitro drug release profile, DOX-loaded Fe_3O_4@CGO–Tau/Glu was transferred into a dialysis bag (molecular weight cut-off: 14 kDa) containing 5 mL of buffer solution. After sealing, the dialysis bag was immersed in a beaker containing 50 mL of phosphate-buffered saline (PBS; pH 7.4 or 6.5) and maintained at 37 °C. At predetermined time intervals, 3 mL aliquots were withdrawn from the release medium and immediately replaced with an equal volume of fresh buffer to maintain a constant volume. All release experiments were performed in triplicate. The amount of DOX released into the medium was quantified using UV–Vis spectroscopy, and the cumulative release percentage at time t was calculated using equation (6) [21].

$$\frac{M_t}{M_\infty}(\%) = \frac{C_t}{C_0} \times 100$$

In this equation, $M_t$and M_∞represent the mass of drug released from the nanocarrier at time t and the total amount of drug loaded onto the nanocarrier, respectively. C_t and C_0 denote the drug concentration released at time t and the initial drug concentration loaded onto the nanocarrier, respectively. The experimental release data were fitted using nonlinear kinetic models, including the zero-order, Higuchi, Korsmeyer–Peppas, and Peppas–Sahlin models, employing *Mathematica* software (version 9.0).

2.8. Drug release kinetics studies

To clarify the release mechanism of DOX from the Fe_3O_4@CGO–Tau/Glu nanosystem, the experimental release data were fitted using nonlinear kinetic models, including the zero-order model (Equation 7), Higuchi model (Equation 8), Korsmeyer–Peppas model (Equation 9), and Peppas–Sahlin model (Equation 10) [22].

$$M_t = k_0\, t$$

$$M_t/M_\infty = k_H \times t^{1/2}$$

$$M_t/M_\infty = K_{KP} \times t^n$$

$$M_t/M_\infty = K_1 t^m + K_2 t^{2m}$$

where M_t represents the amount of drug released at time t, and M_∞ denotes the total amount of drug released at equilibrium. k_0 (h^{-1}), k_H (h$^{-1/2}$) and K_{KP} (h^{-n}) refer to the rate constants of the zero-order, Higuchi, and Korsmeyer–Peppas models, respectively. K_1 (h^{-m}) and K_2 (h^{-2m}) represent the rate constants in the Peppas–Sahlin model.

This open-access article is distributed under the terms of the Creative Commons Attribution Non Commercial 4.0 License (CC BY-NC 4.0).

2.9. Statistical Analysis

All experiments were performed at least in triplicate. For adsorption and release studies, nonlinear regression was used to estimate kinetic parameters. The goodness-of-fit of the models was evaluated using the coefficient of determination (R^2) and the root mean square error (RMSE). The model with the highest R^2 and the lowest RMSE was considered the most appropriate for describing the experimental data.

3. Results and Discussion

3.1. Structural characterizations

3.1.1. FT-IR spectra

Figure 1 shows the Fourier Transform Infrared Spectroscopy (FTIR) spectra of GO, CGO, Fe_3O_4@CGO, Tau, Glu, and Tau/Glu@Fe_3O_4/CGO in the range of 4000–400 cm^{-1}. In the GO spectrum, the broad peak at 3442 cm^{-1} corresponds to the stretching vibration of O–H, and the peak at 1626 cm^{-1} is attributed to the stretching vibration of C=O, which is related to the carboxyl groups. The CGO spectrum shows similar bands at 3422 cm^{-1}, 1607 cm^{-1}, 1409 cm^{-1}, 1391 cm^{-1}, and 1021 cm^{-1}, which are assigned to the stretching vibrations of OH, C=O (carboxylic acids attached to the aromatic ring), C=C, C–OH, and C–O–C, respectively.

In the Fe_3O_4@CGO spectrum, the stretching vibration of the Fe–O bond appears at 586 cm^{-1} [23]. In the Tau spectrum, the peak at 1619 cm^{-1} corresponds to the bending vibration of the N–H group of the amine (–NH_2). Additionally, strong and multiple peaks in the range of 1000–1250 cm^{-1} are attributed to the asymmetric and symmetric stretching vibrations of the sulfonyl group (–SO_3H). In the Glu spectrum, the band at 1539 cm^{-1} is attributed to the bending vibration of the N–H group of the amine.

In the Tau/Glu@Fe_3O_4/CGO spectrum, the absorption band at 1629 cm^{-1} is assigned to the stretching vibrations of amide carbonyl, which indicates the formation of an amide bond between the amine groups (from Tau and Glu) and the carboxylic acid groups of Fe_3O_4@CGO [12]. FTIR analysis results suggest that GO has been successfully functionalized with Tau and Glu. Furthermore, the presence of iron oxide nanoparticles in the Fe_3O_4@CGO structure is confirmed by the stretching vibration of the Fe–O bond. The appearance of the amide carbonyl stretching in the Fe_3O_4@CGO–Tau/Glu spectrum indicates the formation of amide linkages between the amine groups of Tau and Glu and the carboxylic acid groups of Fe_3O_4@CGO.

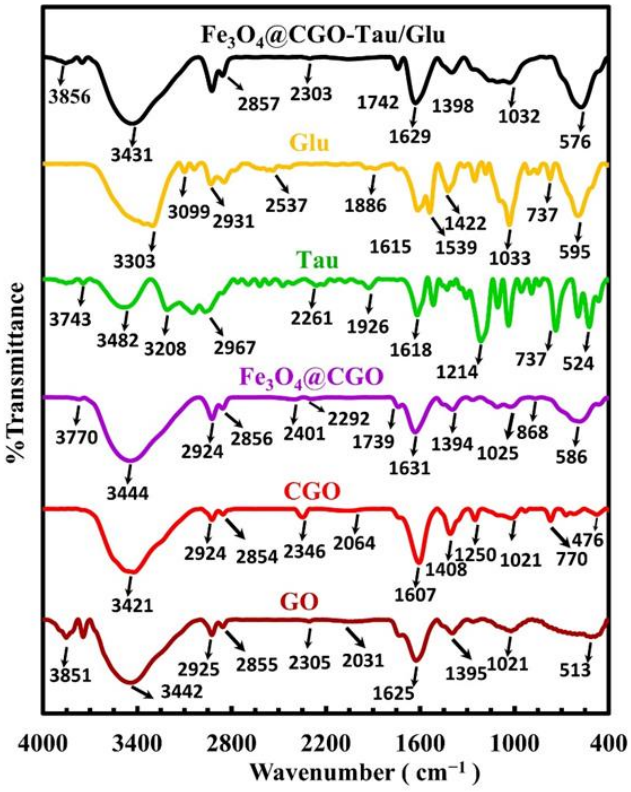


Figure 1. FTIR spectra of GO, CGO, Fe_3O_4@CGO, Tau, Glu, and Fe_3O_4@CGO–Tau/Glu.

3.1.2. XRD analysis

Figure 2 shows the wide-angle X-ray diffractograms (XRD) analysis of CGO, Fe_3O_4@CGO, and Fe_3O_4@CGO–Tau/Glu nanocomposites. In the CGO spectrum, the broad and intense peak at 2θ = 12.4° corresponds to the (001) crystal plane. A weaker peak in the range of 2θ = 27° indicates the presence of some unoxidized and pure graphite. In the XRD pattern of Fe_3O_4@CGO, sharp peaks at 2θ = 30°, 35°, 43°, 57°, and 62° correspond to the (220), (311), (400), (440), and (511) crystal planes, respectively, confirming the cubic structure of Fe_3O_4 [23]. The XRD pattern of the Tau/Glu@Fe_3O_4/CGO nanocomposite also shows distinct sharp peaks at 2θ = 30°, 35°, 43°, 57°, and 65°,

This open-access article is distributed under the terms of the Creative Commons Attribution Non Commercial 4.0 License (CC BY-NC 4.0).

indicating that the crystalline structure of Fe_3O_4 is preserved after surface functionalization.

The XRD analysis of Fe_3O_4@CGO implied the presence of the crystalline Fe_3O_4 phase. These findings are consistent with those reported by Wang et al. [24]. Moreover, the unchanged diffraction pattern of Fe_3O_4@CGO after surface modification with Tau and Glu suggests that the functionalization process did not affect the crystalline structure of Fe_3O_4.

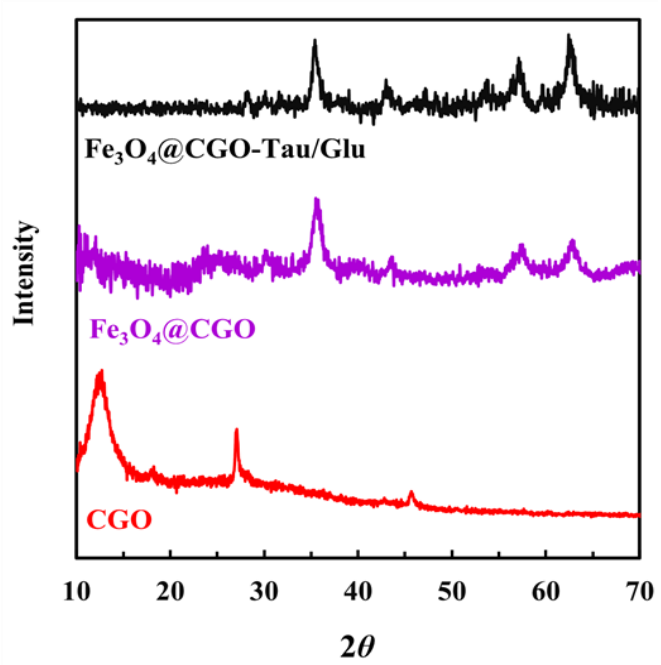


Figure 2. XRD patterns of CGO, Fe_3O_4@CGO, and Fe_3O_4@CGO–Tau/Glu.

3.1.3. VSM analysis

Magnetization can be considered an indicator of a material's magnetic properties. The Vibrating Sample Magnetometer (VSM) provides precise measurements of sample magnetization under varying magnetic field conditions. The changes in magnetic properties for the Fe_3O_4@CGO–Tau/Glu and Fe_3O_4@CGO samples are shown in **Figure 3**. According to the data, the saturation magnetization (Ms) values for Fe_3O_4@CGO and Fe_3O_4@CGO–Tau/Glu are 29.3 emu/g and 30.8 emu/g, respectively. Therefore, both samples exhibit superparamagnetic properties [25].

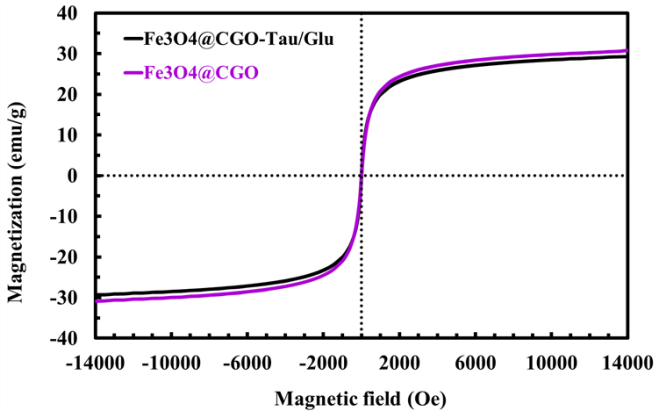


Figure 3. Vibrating sample magnetometer (VSM) magnetization curves of Fe_3O_4@CGO–Tau/Glu and Fe_3O_4@CGO.

3.1.4. Brunauer–Emmett–Teller (BET) and Barrett–Joyner–Halenda (BJH) Analysis

The nitrogen adsorption–desorption isotherms of GO and Fe_3O_4@CGO–Tau/Glu are presented in **Figure 4**, while the corresponding specific surface area, pore volume, and average pore diameter are summarized in **Table 1**. The specific surface area of GO was measured as 539.3 $m^2\ g^{-1}$, with a pore volume of 0.017 $cm^3\ g^{-1}$. Following surface modification with Tau/Glu and formation of the Fe_3O_4@CGO–Tau/Glu nanocomposite, the specific surface area increased to 56.069 $m^2\ g^{-1}$ and the pore volume to 0.136 $cm^3\ g^{-1}$. In contrast, the average pore diameter decreased from 19.31 nm for GO to 9.678 nm for Fe_3O_4@CGO–Tau/Glu.

The BET and BJH results suggest that functionalization of Fe_3O_4@CGO with Tau/Glu leads to an increase in specific surface area and pore volume, accompanied by a reduction in average pore diameter. The noticeable decrease in pore size suggests a shift from larger, less uniform pores to smaller, more homogeneous pores. Such structural evolution may increase the effective contact area between the nanocarrier surface and drug molecules, thereby favoring surface adsorption.

Table 1. Comparison of the porous characteristics of GO and Fe_3O_4@CGO–Tau/Glu

Material	GO	Fe_3O_4@CGO-Tau/Glu
BET surface area ($m^2\ g^{-1}$)	3.539	56.069
Pore volume ($cm^3\ g^{-1}$)	0.017	0.136
Mean pore diameter (nm)	19.31	9.678

This open-access article is distributed under the terms of the Creative Commons Attribution Non Commercial 4.0 License (CC BY-NC 4.0).

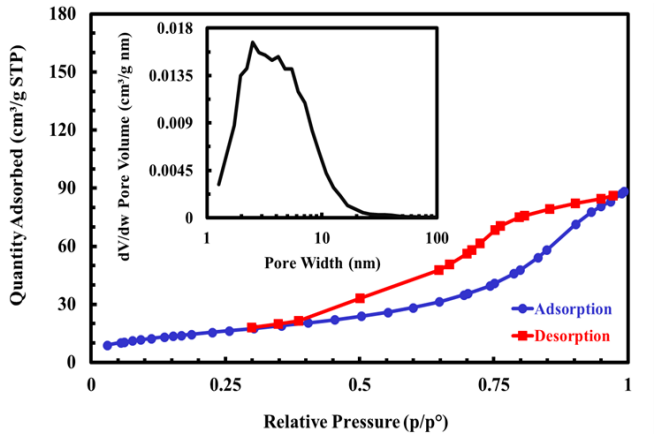


Figure 4. Adsorption-desorption isotherms of GO and Fe_3O_4@CGO–Tau/Glu.

3.1.5. FE-SEM analysis

The surface morphology and size of CGO, Fe_3O_4@CGO, and Fe_3O_4@CGO–Tau/Glu were examined using field-emission scanning electron microscopy (FE-SEM) (**Figure 5**). The images (a–c) reveal the thin, layered, and wrinkled morphology of CGO nanosheets, which is characteristic of graphene-based materials.

In the Fe_3O_4@CGO images (d–f), Fe_3O_4 nanoparticles are observed to be distributed over the graphene sheets, resulting in increased surface roughness and heterogeneity. After surface modification with Tau/Glu, a reduced tendency toward particle aggregation is observed (images g–i), which may be attributed to the presence of organic functional groups that alter surface interactions.

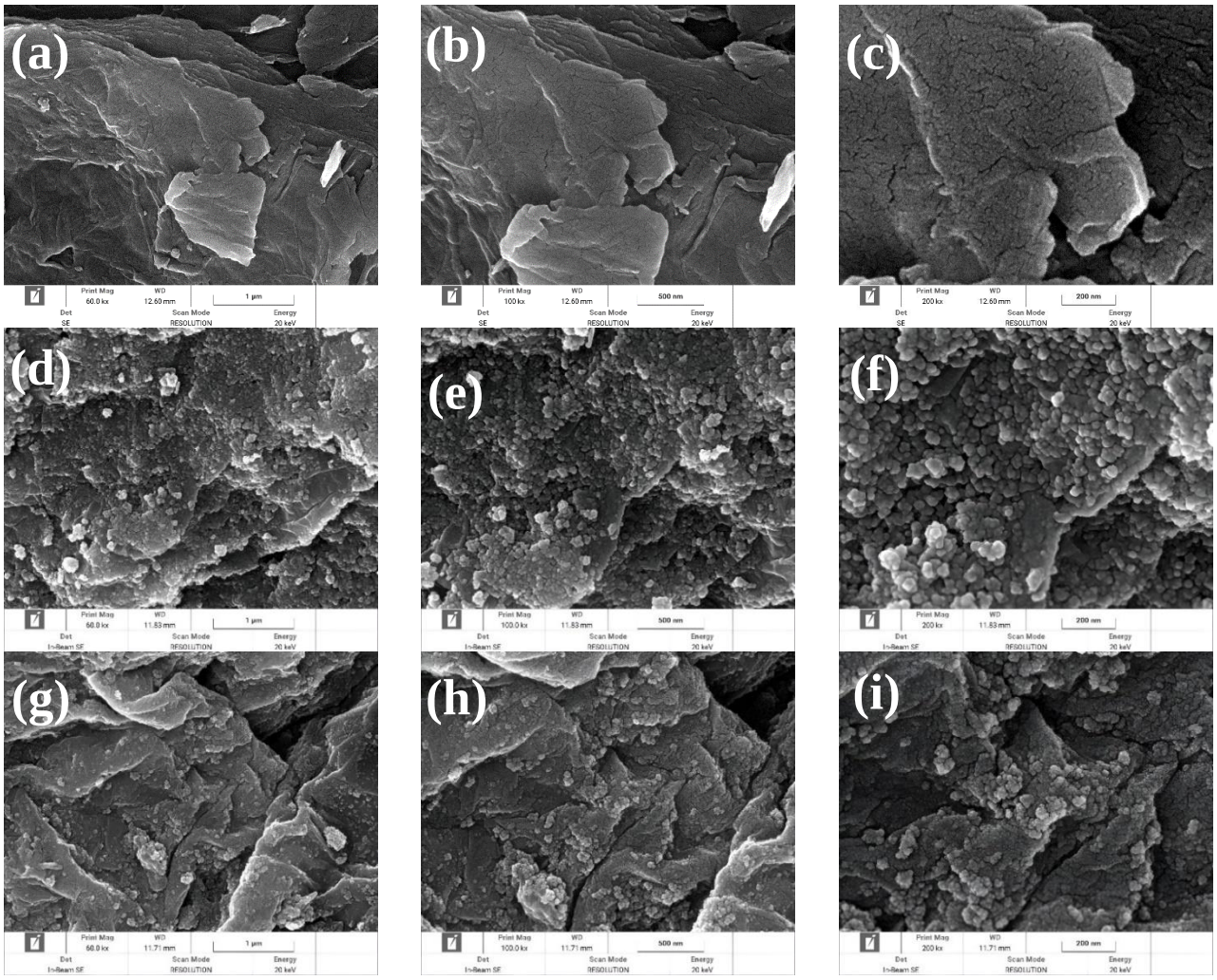


Figure 5. FESEM images at magnifications of 1 µm, 500 nm, and 200 nm from left to right. (a–c) CGO, (d–f) Fe_3O_4@CGO, (g–i) Fe_3O_4@CGO–Tau/Glu.

This open-access article is distributed under the terms of the Creative Commons Attribution Non Commercial 4.0 License (CC BY-NC 4.0).

3.2. Effect of pH on adsorption

The initial solution pH plays a key role in determining the nanocarrier's surface charge and its interaction with drug molecules. At the point of zero charge ($pH_{_pzc}$), the adsorbent surface is electrically neutral; at pH values above pH_pzc, the surface becomes negatively charged, whereas at pH values below pH_pzc, it becomes positively charged. As shown in **Figure 6**, the pH_{pzc} of Fe_3O_4@CGO–Tau/Glu was determined to be 4.45. Accordingly, the nanocarrier surface is positively charged at pH < 4.45 and negatively charged at pH > 4.45.

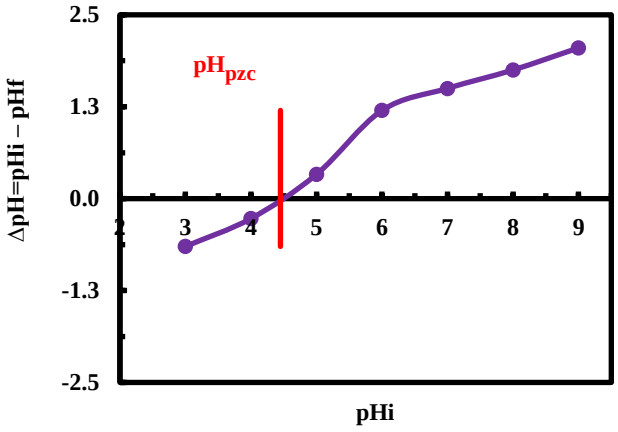


Figure 6. pH_{pzc} curve of Fe_3O_4@CGO–Tau/Glu.

The effect of pH on DOX adsorption was investigated over the pH range of 3–9 (**Figure 7**). Relatively low adsorption capacities were observed under acidic conditions, which may be attributed to electrostatic repulsion between the positively charged adsorbent surface and cationic DOX species. With increasing pH, the adsorption capacity increased progressively and reached a maximum at pH = 8. At this pH, the nanocarrier surface is negatively charged while DOX predominantly exists in a cationic form, leading to, while DOX predominantly exists in a cationic form, resulting in enhanced electrostatic attraction and, consequently, maximum adsorption. Under these conditions, an adsorption capacity of 37.07 mg g^{-1} and a LE of 92.68% were obtained.

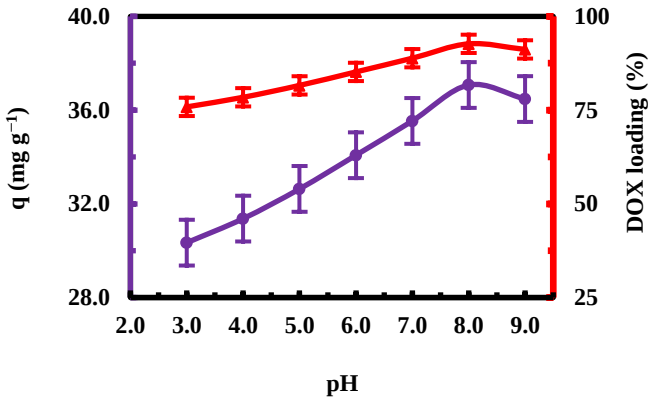


Figure 7. Effect of pH on drug loading percentage and adsorption capacity of Fe_3O_4@CGO-Tau/Glu.

3.3. Adsorption kinetics

A comprehensive kinetic evaluation was conducted to characterize the adsorption behavior of DOX onto Fe_3O_4@CGO–Tau/Glu. Based on the kinetic parameters summarized in **Table 2**, the PSO model provided the best fit to the experimental data. As shown in **Figure 8**, this is reflected by high correlation coefficients (R^2 = 0.999) and low RMSE values (0.0259–0.0825) for all adsorbent dosages. An increase in adsorbent dosage from 5 to 20 mg led to an increase in the k_2 value from 0.017 to 0.073 g mg^{-1} min^{-1}, indicating faster adsorption kinetics and shorter equilibrium times. Conversely, the adsorption capacity ($q_{e,cal}$, mg g^{-1}) decreased from 73.053 to 19.661 mg g^{-1} with increasing adsorbent dosage. The decrease in $q_{e,cal}$ with increasing adsorbent dosage can be attributed to the distribution of a fixed amount of DOX molecules over a larger number of available adsorption sites. As the adsorbent dosage increases, the drug molecules are partitioned among more active sites, resulting in a lower amount of drug adsorbed per unit mass of adsorbent. Furthermore, at higher dosages, possible particle aggregation of active sites may reduce the effective surface area accessible for adsorption.

Although the $q_{e,\ cal}$ values obtained from the PFO model (71.08, 36.35, and 19.08 mg g^{-1}) are relatively close to the experimental values, their deviation from $q_{e,exp}$ is larger than that of the PSO model, indicating lower accuracy in describing the adsorption process.

This open-access article is distributed under the terms of the Creative Commons Attribution Non Commercial 4.0 License (CC BY-NC 4.0).

Table 2. Parameters of nonlinear kinetic models for the adsorption process of DOX onto Fe_3O_4@CGO–Tau/Glu at different adsorbent amounts.

Kinetic models	Parameters	Dosage of adsorbent (mg)		
		5	10	20
Pseudo-first-order	K_1 (min^{-1})	0.418	0.436	0.458
	$q_{e,cal}$ (mg g^{-1})	71.084	36.347	19.079
	R^2	0.9997	0.9996	0.9997
	RMSE	1.2872	0.6832	0.3025
Pseudo-second-order	K_2 (g $mg^{-1}min^{-1}$)	0.017	0.035	0.073
	$q_{e,cal}$ (mg g^{-1})	73.053	37.432	19.661
	R^2	0.9999	0.9999	0.9999
	RMSE	0.0455	0.0825	0.0259
Intra-particle diffusion	K_i (mg $g^{-1}min^{-1/2}$)	1.039	0.605	0.344
	C_i (mg g^{-1})	63.993	32.571	17.120
	R^2	0.9995	0.9996	0.9997
	RMSE	1.5022	0.6771	0.3378
	$q_{e,exp}$ (mg g^{-1})	72.472	37.178	19.476

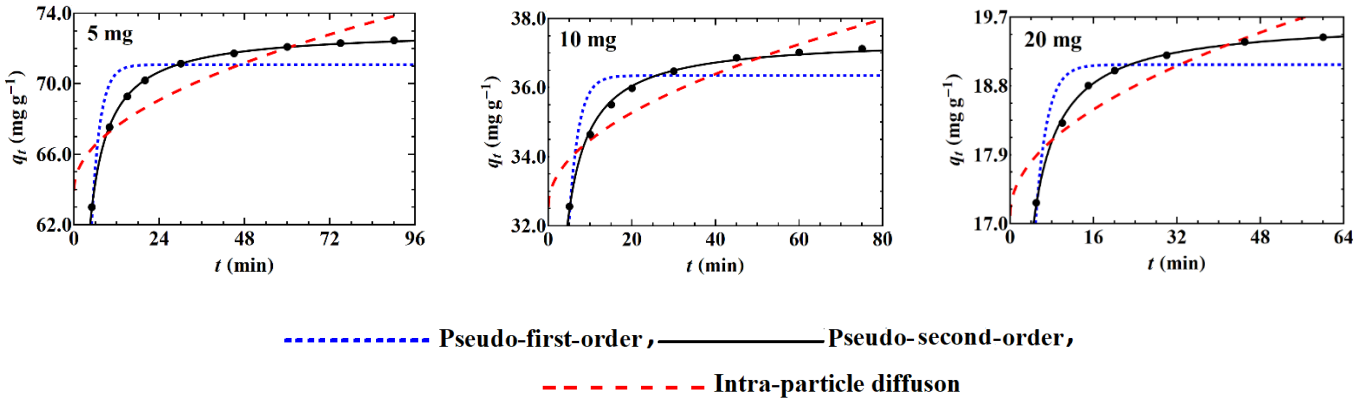


Figure 8. Nonlinear plots of kinetic models for the adsorption process of DOX onto Fe_3O_4@CGO–Tau/Glu at different adsorbent dosages.

The IPD model also exhibited high R^2 values (0.9995–0.9997); however, its higher RMSE values (0.816–4.514) compared with the PSO model indicate greater deviation from the experimental data. The decrease in k_i from 1.04 to 0.34 mg g^{-1} $min^{-1/2}$ with increasing adsorbent dosage suggests slower diffusion at higher dosages. Moreover, the positive intercept values (C_i = 17.12–63.99 mg g^{-1}) imply that surface adsorption on the external layer plays a significant role in mass transfer, and intraparticle diffusion is not the sole rate-controlling mechanism [26].

The kinetic analysis demonstrates that DOX adsorption onto Fe_3O_4@CGO–Tau/Glu is best described by the PSO model, whereas the PFO model provides a less accurate description. The observed decrease in adsorption capacity at higher adsorbent dosages may be attributed to a reduced drug-to-active-site ratio, partial blockage of adsorption sites due to particle aggregation, and increased mass-transfer resistance arising from the formation of dense adsorption layers. Therefore, the adsorption mechanism is governed by a combination of surface interactions and intraparticle diffusion.

This open-access article is distributed under the terms of the Creative Commons Attribution Non Commercial 4.0 License (CC BY-NC 4.0).

3.4. In vitro drug release profile

Figure 9 illustrates the release profiles of DOX from the Fe_3O_4@CGO–Tau/Glu nanocarrier under tumor-mimicking (pH 6.5) and physiological (pH 7.4) conditions. The results demonstrate a faster release rate and a higher cumulative release under acidic conditions than in a neutral medium. Within the first 30 min, approximately 11% of DOX was released at pH 6.5, whereas only 6% was released at pH 7.4. After 6 h, the cumulative release reached 47% in the acidic medium, compared with 17% under physiological conditions. As the release progressed, the difference between the two pH environments became more pronounced; after 12 and 24 h, the cumulative release at pH 6.5 increased to 64% and 74%, respectively, whereas it reached 24% and 31% at pH 7.4. After 48 h, the total DOX release under acidic conditions reached 86%, whereas it remained limited to 36% at physiological pH.

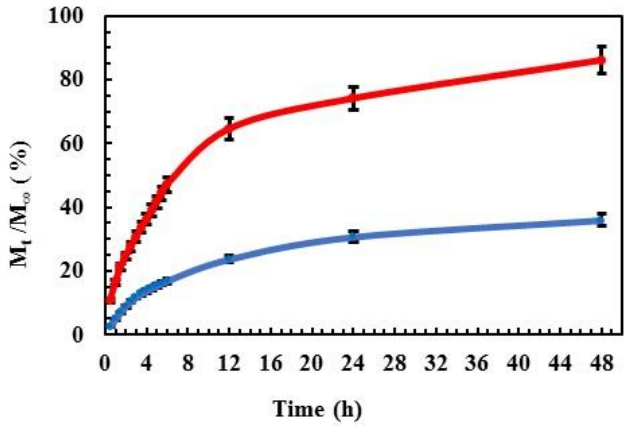


Figure 9. DOX release profile from Fe_3O_4@CGO–Tau/Glu at pH 6.5 and 7.4 over 48 hours.

The distinct release behavior of DOX from the Fe_3O_4@CGO–Tau/Glu system can be attributed to the combined effects of surface charge, surface functional groups, and the drug's molecular form. Considering the pH_{pzc} value of 4.45, the nanocarrier surface is negatively charged at both pH 6.5 and 7.4, while DOX predominantly exists in its cationic form (approximately 40% at pH 6.5 and 65% at pH 7.4). Although electrostatic attraction between the nanocarrier and DOX is present under both conditions, protonation of residual carboxylate groups at acidic pH weakens these interactions. In addition, competition between protons and DOX molecules for hydrogen bonding with surface hydroxyl and carbonyl groups further reduces drug–carrier interactions, thereby accelerating drug release under acidic conditions.

In contrast, at physiological pH, the lower proton concentration favors stronger hydrogen bonding between the non-ionized fraction of DOX and the hydroxyl and carbonyl groups on the Fe_3O_4@CGO–Tau/Glu surface, resulting in slower and more controlled drug release. These findings show that the designed nanocarrier enables pH-dependent and controlled release of DOX. This behavior is consistent with previous reports; for instance, Zamani et al. demonstrated that DOX release from monochlorotriazinyl β-cyclodextrin derivatives is significantly faster at acidic pH than at physiological pH 7.4 [27].

Similar pH-dependent release behavior has also been reported in magnetic graphene-based delivery systems structurally comparable to the present nanocarrier. For example, the in vitro release behavior of DOX from Triazine dendrimer-conjugated graphene quantum dots (GQDs) immobilized on Fe_3O_4@C@NH_2 core-shell (Fe_3O_4@C@TDGQDs) microspheres was evaluated in PBS at different pH values and over various time intervals at 37°C. The cumulative DOX release reached approximately 65.09% under mildly acidic conditions (pH 5.0), whereas only 28.48% was released at near-neutral pH (7.4) after 72 h [28]. These findings highlight that the pH-responsive release profile is predominantly governed by the nanocarrier's physicochemical characteristics and surface functionalities rather than the intrinsic properties of DOX alone.

3.4.1 Drug release kinetics

The in vitro release profiles were analyzed by fitting the experimental data to several nonlinear kinetic models, namely the zero-order, Higuchi, Korsmeyer–Peppas, and Peppas–Sahlin models. The resulting fitting curves are illustrated in **Figure 10**, and the corresponding kinetic parameters derived from the models are listed in **Table 3**.

This open-access article is distributed under the terms of the Creative Commons Attribution Non Commercial 4.0 License (CC BY-NC 4.0).

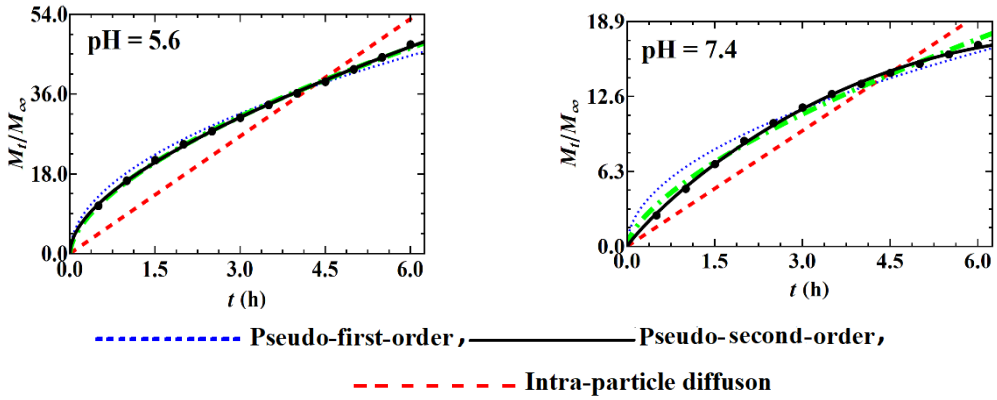


Figure 10. Nonlinear kinetic models of DOX release from DOX@Fe_3O_4@CGO–Tau/Glu at pH 6.5 and 7.4 at 37 °C.

Table 3. Parameters of nonlinear kinetic models for DOX release from DOX@Fe_3O_4@CGO–Tau/Glu at pH 6.5 and 7.4 at 37 °C.

Kinetics model	Parameters	pH value	
		5.6	7.4
Zero-order	k_0 (h^{-1})	8.835	3.247
	R^2	0.9751	0.9802
	RMSE	5.1942	1.7000
Higuchi	k_H ($h^{-1/2}$)	18.247	6.674
	R^2	0.9982	0.9936
	RMSE	1.3761	0.9641
Korsmeyer-Peppas	K_{KP} (h^{-n})	16.230	5.452
	n	0.587	0.645
	R^2	0.9999	0.9985
	RMSE	0.3537	0.4652
Peppas-Sahlin	K_1 (h^{-n})	14.859	5.395
	K_2(h^{-2n})	1.522	−0.413
	n	0.512	0.905
	R^2	0.9999	0.9998
	RMSE	0.3001	0.1552

The nonlinear kinetic analysis demonstrated that the Korsmeyer–Peppas and Peppas–Sahlin models provided the best fit to the experimental DOX release data under both tumor-mimicking (pH 6.5) and physiological (pH 7.4) conditions. For the Korsmeyer–Peppas model, the correlation coefficients (R^2) were 0.9999 at pH 6.5 and 0.9985 at pH 7.4, with corresponding RMSE values of 0.3537 and 0.4652, respectively, suggesting a reliable description of the release behavior.

The release exponent (n) was calculated as 0.587 under acidic conditions and 0.465 at physiological pH, while the release rate constant (k) reached 16.230 h^{-n} and 5.452 h^{-n}, respectively. The higher K_{KP} value at acidic pH indicates accelerated DOX release under tumor-mimicking conditions. The n values within the range of 0.45–0.89 suggest that DOX release follows a non-Fickian, or anomalous, mechanism, in which both diffusion and polymer matrix swelling/erosion contribute to drug release.

To quantitatively distinguish the relative contribution of each process, the experimental data were further analyzed using the Peppas–Sahlin model. Very high correlation coefficients (R^2 = 0.9999) and extremely low RMSE values (0.3001 at pH 6.5 and 0.1552 at pH 7.4) confirm the excellent predictive capability of this model.

In the Peppas–Sahlin model, the term K_1t^m represents the contribution of Fickian diffusion, whereas K_2t^{2m} accounts for polymer relaxation or matrix swelling/erosion [29]. Under both pH conditions, the diffusion-related rate constant (K_1) was significantly higher than the swelling/erosion-related constant (K_2),

This open-access article is distributed under the terms of the Creative Commons Attribution Non Commercial 4.0 License (CC BY-NC 4.0).

implying that diffusion predominates as the main rate-controlling mechanism. Therefore, the DOX release from the Fe_3O_4@CGO–Tau/Glu nanosystem can be characterized as anomalous transport, with a dominant Fickian diffusion mechanism.

Overall, although both diffusion and swelling/erosion contribute to the release process, diffusion plays the predominant role. These findings are consistent with the results reported by Bakhshi et al., who demonstrated that DOX release from chitosan/hydroxyapatite-based magnetic hydrogels is primarily controlled by Fickian diffusion [30].

4. Conclusions

The findings of this study suggest that the Fe_3O_4@CGO–Tau/Glu system has the potential to serve as a pH-responsive nanocarrier, facilitating efficient DOX loading and controlled release. Spectroscopic and structural analyses indicated that functionalization with Tau and Glu enhances the dispersion of Fe_3O_4 nanoparticles, increases the specific surface area, and alters the pore structure towards smaller and more uniform pores, thereby improving drug adsorption efficiency.

Kinetic analyses revealed that the PSO model best describes DOX adsorption, while the release behavior follows the Korsmeyer–Peppas and Peppas–Sahlin models, with Fickian diffusion identified as the dominant rate-controlling mechanism. These characteristics, coupled with the superparamagnetic behavior of the structures, may hold potential for magnetically guided targeting and controlled release. However, certain limitations must be acknowledged. The nanosystem's performance was not evaluated in more complex biological environments, such as plasma, blood, or the actual tumor microenvironment. Moreover, long-term stability and possible interactions with serum proteins or healthy cells were not explored. Therefore, further in vitro and in vivo studies are essential to evaluate the biosafety, circulation stability, and antitumor efficacy of this nanosystem.

Conflict of interest

The authors declare no competing interests.

Data availability

All relevant data are included within the manuscript.

Authors Contributions

Seyyed Mostafa Hosseini: material preparation, investigation, data collection, resources, validation, and writing—original draft. Parisa Miralinaghi: conceptualization, research goal definition, writing—original draft, supervision, and project administration. Mahsasadat Miralinaghi: methodology, investigation, data analysis, supervision, project administration, and review & editing. Mohammadjavad Sohrabi: methodology, data analysis, and review & editing.

Authors Orcid numbers:

Seyyed Mostafa Hosseini: https://orcid.org/0009-0009-6606-676X
Parisa Miralinaghi: https://orcid.org/0000-0002-6097-3344
Mahsasadat Miralinaghi: https://orcid.org/0000-0002-7629-6464
Mohammadjavad Sohrabi: https://orcid.org/0000-0002-3429-5383

Funding

This research did not receive any specific grant from funding agencies in the public, commercial, or not-for-profit sectors.

Using artificial intelligence chatbots

Artificial intelligence chatbots were used solely to assist with language editing, translation, and structural refinement of the manuscript. All scientific content, experimental design, data analysis, interpretation of results, and conclusions were conceived, verified, and finalized by the authors.

References

1. Senapati S, Mahanta AK, Kumar S, Maiti P. Controlled drug delivery vehicles for cancer treatment and their performance. Signal Transduct. Target. Ther. (2018) 3: 1–19.
2. Liu J, Yi X, Zhang J, Yao Y, Panichayupakaranant P, Chen H. Recent Advances in the Drugs and Glucose-Responsive Drug Delivery Systems for the Treatment of Diabetes: A Systematic Review. Pharmaceutics (2024) 16: 1343.

This open-access article is distributed under the terms of the Creative Commons Attribution Non Commercial 4.0 License (CC BY-NC 4.0).

3. Song Y, Jing H, Vong LB, Wang J, Li N. Recent advances in targeted stimuli-responsive nano-based drug delivery systems combating atherosclerosis. Chin. Chem. Lett. (2022) 33: 1705–17.
4. Sun Y, Davis E. Nanoplatforms for Targeted Stimuli-Responsive Drug Delivery: A Review of Platform Materials and Stimuli-Responsive Release and Targeting Mechanisms. Nanomater. (2021) 11(3): 746.
5. Sui Y, Shen Z, Wang Z, Feng J, Zhou G. Lactylation in cancer: metabolic mechanism and therapeutic strategies. Cell Death Discov. (2025) 11:1–9.
6. Kaushik NNKN, Borkar SB, Nandanwar SK, Panda PK, Choi EH, Kaushik NNKN. Nanocarrier cancer therapeutics with functional stimuli-responsive mechanisms. J. Nanobiotechnology (2022) 20: 1–23.
7. Mansoori B, Mohammadi A, Davudian S, Shirjang S, Baradaran B. The Different Mechanisms of Cancer Drug Resistance: A Brief Review. Adv. Pharm. Bull. (2017) 7: 339–48.
8. Nogueira J, Soares SF, Amorim CO, Amaral JS, Silva C, Martel F, et al. Magnetic Driven Nanocarriers for pH-Responsive Doxorubicin Release in Cancer Therapy. Molecules (2020) 25: 333.
9. Kar A, Agarwal S, Singh A, Bajaj A, Dasgupta U. Insights into molecular mechanisms of chemotherapy resistance in cancer. Transl. Oncol. (2024) 42: 101901.
10. Radu ER, Semenescu A, Voicu SI. Recent Advances in Stimuli-Responsive Doxorubicin Delivery Systems for Liver Cancer Therapy. Polymers (2022) 14: 5249.
11. Renu K, V.G. A, Tirupathi TP, Arunachalam S. Molecular mechanism of doxorubicin-induced cardiomyopathy – An update. Eur. J. Pharmacol. (2018) 818: 241–53.
12. Pan H, Yu Y, Li L, Liu B, Liu Y. Fabrication and Characterization of Taurine Functionalized Graphene Oxide with 5-Fluorouracil as Anticancer Drug Delivery Systems. Nanoscale Res. Lett. (2021) 16: 1–13.
13. Mohammed-Ahmed HK, Nakipoglu M, Tezcaner A, Keskin D, Evis Z. Functionalization of graphene oxide quantum dots for anticancer drug delivery. J. Drug Deliv. Sci. Technol. (2023) 80: 104199.
14. Zhong Y, Guo F, Feng W, Shang X, Chen Y. A novel drug delivery system based on amorphous zeolite derived from kanemite and its sustained release of doxorubicin. Res. Chem. Intermed. (2026) 52: 1537–1558.
15. Hosseini S M, Miralinaghi P, Miralinaghi M MH. Synthesis and evaluation of the cytotoxic and hemolytic effects of taurine/glucosamine-functionalized graphene oxide nanosheets for doxorubicin drug delivery. J Ilam Uni. Med. Sci. (2025) 33: 131.
16. Pooja D, Srinivasa Reddy T, Kulhari H, Kadari A, Adams DJ, Bansal V, et al. N-acetyl-d-glucosamine-conjugated PAMAM dendrimers as dual receptor-targeting nanocarriers for anticancer drug delivery. Eur. J. Pharm. Biopharm. (2020) 154: 377–86.
17. Tran TT Van, Tran ML, Nguyen CH. Carboxylated graphene oxide: Characterization change and enhanced adsorption capacity towards Pb^{2+} and Cu^{2+} in wastewater. J. Mol. Liq. (2025) 426: 127312.
18. Momeni S, Ghorbani-Vaghei R. Novel modified magnetic graphene oxide as an efficient and green catalyst for one-pot synthesis of pyrazoles. Sci. Rep. (2025) 15:1–20.
19. Althumayri K, Guesmi A, Abd El-Fattah W, Khezami L, Soltani T, Hamadi N Ben, et al. Effective Adsorption and Removal of Doxorubicin from Aqueous Solutions Using Mesostructured Silica Nanospheres: Box–Behnken Design Optimization and Adsorption Performance Evaluation. ACS Omega (2023) 8: 14144–59.
20. Shaha CK, Mahmud MA Al, Saha S, Karmaker S, Saha TK. Efficient removal of sparfloxacin antibiotic from water using sulfonated graphene oxide: Kinetics, thermodynamics, and environmental implications. Heliyon (2024) 10: e33644.
21. Karimi S, Zeyni V, Namazi H. A fluorescent system based on graphene quantum dots-capped magnetic hydroxyapatite-MIL-100 metal-organic frameworks for pH-sensitive and controlled release of DOX. Diam. Relat. Mater. (2023) 140:110502.
22. Wójcik-Pastuszka D, Krzak J, Macikowski B, Berkowski R, Osiński B, Musiał W. Evaluation of the Release Kinetics of a Pharmacologically Active Substance from Model Intra-Articular Implants Replacing the Cruciate Ligaments of the Knee. Materials (Basel) (2019) 12(8): 1202.
23. Perveen S, Nadeem R, Iqbal M, Bibi S, Gill R, Saeed R, et al. Graphene oxide and Fe3O4 composite synthesis, characterization and adsorption efficiency evaluation for $NO3^{-}$ and $PO43^{-}$ ions in aqueous medium. J. Mol. Liq. (2021) 339: 116746.
24. Wang G, Chen G, Wei Z, Dong X, Qi M. Multifunctional Fe3O4/graphene oxide nanocomposites for magnetic resonance imaging and drug delivery. Mater.. Chem. Phys (2013) 141: 997–1004.
25. Abbasi Z, Farrokhnia A, Garcia-Lopez EI, Zargar Shoushtari M, Aghaie E. Synthesis of ZnO–Ag2CO3–Fe3O4@rGO core–shell structure: magnetically separable photocatalyst for degradation of MB using the Box–Behnken design. J. Mater. Sci.: Mater. Electron. (2020) 31: 19554–68.

This open-access article is distributed under the terms of the Creative Commons Attribution Non Commercial 4.0 License (CC BY-NC 4.0).

26. Vega MF, Díaz-Faes E, Barriocanal C. Kinetic and mechanistic study of CO2 adsorption on activated hydrochars. Journal of CO2 Util. (2024) 81: 102716.
27. Zamani F, Dinari M, Yazdani A, Asadi P. Monochlorotriazinyl-β-cyclodextrin as a promising nanocarrier for pH-responsive doxorubicin delivery: Simulation and experimental validation. Carbohydr. Polym. Technol. Appl. (2025) 10: 100876.
28. Karimi S, Namazi H. Simple preparation of maltose-functionalized dendrimer/graphene quantum dots as a pH-sensitive biocompatible carrier for targeted delivery of doxorubicin. Int J. Biol. Macromol. (2020) 156: 648–59.
29. Aykin-Dinçer E, Dincer C, Topuz OK. Modeling of Release Mechanism of Sage (Salvia fruticosa Miller) Phenolics Encapsulated in Alginate Capsule: Physicochemical Properties. J. Food Process. Preserv. (2024) 2024(1):7598455.
30. Alemi F, Maleki M, Mir M, Ebrahimi-Kalan A, Zarei M, Yousefi B, et al. Synthesis, characterization, and evaluation of pH-sensitive doxorubicin-loaded functionalized graphene oxide in osteosarcoma cells. Bioimpacts (2023) 13: 207–18.

This open-access article is distributed under the terms of the Creative Commons Attribution Non Commercial 4.0 License (CC BY-NC 4.0).